

---

# Few-Shot Learning by Explicit Physics Integration: An Application to Groundwater Heat Transport

---

**Julia Pelzer**

Institute for Parallel and Distributed Systems  
University of Stuttgart  
Stuttgart, Germany  
julia.pelzer@ipvs.uni-stuttgart.de

**Corné Verburg**

Delft Institute of Applied Mathematics  
Delft University of Technology  
Delft, the Netherlands  
c.verburg@tudelft.nl

**Alexander Heinlein**

Delft Institute of Applied Mathematics  
Delft University of Technology  
Delft, the Netherlands  
a.heinlein@tudelft.nl

**Miriam Schulte**

Institute for Parallel and Distributed Systems  
University of Stuttgart  
Stuttgart, Germany  
miriam.schulte@ipvs.uni-stuttgart.de

## Abstract

Machine learning methods often struggle with real-world applications in science and engineering due to limited or low-quality training data. In this work, the example of groundwater flow with heat transport is considered; this corresponds to an advection-diffusion process under heterogeneous flow conditions, that is, spatially distributed material parameters and heat sources. Classical numerical simulations are costly and challenging due to high spatio-temporal resolution requirements and large domains. While often computationally more efficient, purely data-driven surrogate models face difficulties, particularly in predicting the advection process, which is highly sensitive to input variations and involves long-range spatial interactions. Therefore, in this work, a Local-Global Convolutional Neural Network (LGCNN) approach is introduced. It combines a lightweight numerical surrogate for the transport process (global) with convolutional neural networks for the groundwater velocity and heat diffusion processes (local). With the LGCNN, a city-wide subsurface temperature field is modeled, involving a heterogeneous groundwater flow field and one hundred groundwater heat pump injection points forming interacting heat plumes over long distances. The model is first systematically analyzed based on random subsurface input fields. Then, the model is trained on a handful of cut-outs from a real-world subsurface map of the Munich region in Germany, and it scales to larger cut-outs without retraining. All datasets, our code, and trained models are published for reproducibility.

## 1 Introduction

Many real-world systems, across environmental engineering, geoscience, and biomedicine, feature transport phenomena governed by coupled advection–diffusion processes, e.g., pollutant transport through air or water, chemical reactions, or heat transport in flowing media. In such settings, interactions can span large distances, long timescales and many components.

Datasets based on physical measurements are often limited by cost, logistics, or experimental constraints. While numerical simulations can address these limitations to some extent, they become impractically slow or computationally expensive as domain size or resolution increases. Machine learning (ML) models offer fast predictions but typically require large training datasets and often struggle to scale to larger domains. This trade-off underscores the need for data-efficient surrogates that can capture both local and long-range interactions, and scale to arbitrary domain sizes and numbers of interacting components. To this end, we introduce the **Local-Global Convolutional Neural Network (LGCNN)**, a scalable, physics-inspired approach that leverages the structure of advection-diffusion problems by decoupling local and global transport processes.

We apply this approach to the climate change-relevant application of modeling city-wide subsurface temperature fields driven by heat and mass injections of dozens of open-loop groundwater heat pumps (GWHP)[29, 11, 14] in the region of Munich, Germany[51]. A city-wide optimization of the positions of all GWHPs requires calling a prediction model dozens of times with slightly adapted GWHP positions to minimize negative interactions between different heat plumes and pumps. For this scenario, our model should predict the temperature field  $T$  in an arbitrarily large domain based on the inputs of the subsurface parameters of a hydraulic pressure gradient  $\nabla p$  and a heterogeneous subsurface permeability field  $k$ , and arbitrary heat pump locations  $i$ . Labels are generated by expensive simulations, but only for a small number of cases and entirely offline.

As sketched in Figure 1, the LGCNN uses CNNs where they excel, and simple numerical surrogates where CNNs struggle: a first CNN predicts the velocities  $\vec{v}$  from local relations of the inputs  $p$ ,  $k$  and  $i$  (Step 1); a fast numerical component calculates the streamlines  $\vec{s}$  based on this (Step 2); a second CNN calculates the temperature distribution  $T$  in the whole domain based on all prior inputs and outputs (Step 3). Since Step 2 covers all non-local effects, Step 3 can again take advantage of CNNs to learn local patterns. We outline related work in Section 2, then define our datasets and metrics in Section 3.

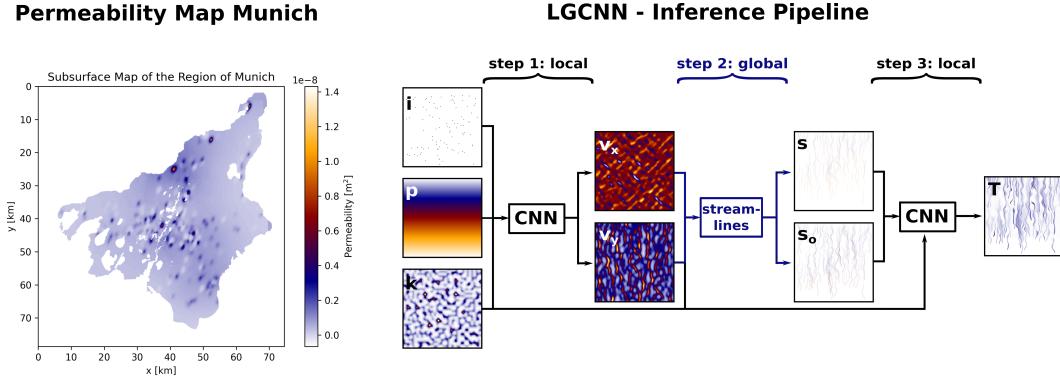


Figure 1: Left: Map of  $k$  of whole region of Munich. Right: Schematics of our Local-Global CNN-based approach (LGCNN) with 3 physics-inspired steps: CNN ( $pki \rightarrow \vec{v}$ ), simplified solver ( $i\vec{v} \rightarrow \vec{s}$ ), CNN ( $pkiv\vec{s} \rightarrow T$ ).

In Section 4, we benchmark purely data-driven models and show their performance and limitations on this low-data challenge. To address data scarcity, we introduce LGCNN in Section 5. Section 6 emphasizes generalization and scalability from a single datapoint, while Section 7 demonstrates transfer to real-world subsurface parameters extracted from measurement maps such as in Figure 1.

**Contributions** Our method strongly reduces data requirements for modeling complex scenarios, increases reliability, and ensures scalability to larger domains by a domain-specific modular design of physics-aided machine learning for an input-sensitive scenario with long-distance effects. Subsurface temperature prediction serves as our example application, with the approach expected to generalize to related domains.

**Limitations** The current approach is limited to two-dimensional and steady-state datasets.

## 2 Related Work

Deep learning surrogates in scientific modeling can be broadly categorized into purely data-driven architectures, physics-informed or domain-structured models, and highly problem-specific hybrid approaches. In this section, we summarize the developments in each category and existing efforts in GWHP modeling.

Convolutional Neural Networks (CNNs), particularly UNet [35] variants, are widely used for spatial prediction tasks due to their locality-aware architecture of moving-window-like kernels. Applications include flow around airfoils [43] and various engineering systems [17]. For general reviews on ML in scientific and real-world engineering contexts, see [38, 36, 3].

To improve generalization and reduce data requirements, domain-structured models embed physical priors or symmetries into their architecture. This includes Fourier Neural Operators (FNOs) for efficient multi-scale modeling [20, 6], thermodynamics-preserving networks [15], and rotation-equivariant CNNs (ECNNs) [48]. Physics-Informed Neural Networks (PINNs) go further by replacing data loss with physics-based constraints, allowing for training without labeled data [31, 7], and have been applied to fluid dynamics and inverse problems [32, 40, 5].

Hybrid approaches combine architectures and integrate domain or physics knowledge to improve general models, for instance, in low-data regimes. Examples include staged CNNs for atmospheric plume dispersion [12], physics-informed FNOs for traffic flow [42], CNN-MLP hybrids for optimizing positions of oil wells [49], and physics-guided CNNs for seismic response prediction [50].

**Deep Learning for GWHP Modeling** In the context of groundwater modeling with heat transport, recent work focuses on isolated or pairwise interacting GWHPs. Most use UNet-based architectures, optionally with physics-loss terms [8, 27, 37]. Although effective in simple, homogeneous aquifers, these models rely on large training datasets or simulated inputs and have not been scaled to city-wide domains with many pumps. UNets are the dominant architecture because of their strong performance on spatial data, making them the baseline for comparison.

We briefly evaluated PINNs and FNOs as alternatives. PINNs, while promising for low-data fluid dynamics tasks [32, 40, 5, 41], struggled with complex scenarios (cf. [19]) such as heterogeneous media and discontinuous source terms in preliminary tests. FNOs, though capable of modeling local and global dependencies, struggled with large domain sizes due to high memory requirements. Additionally, they performed poorly in the presence of multiple sources, consistent with [23].

## 3 Datasets and Metrics

**Datasets** Inputs for the neural networks consist of a heterogeneous permeability field  $k$ , an initial hydraulic pressure field  $p$ , and a one-hot-encoded field of heat pump positions  $i$ . The (interim) labels of velocity  $\vec{v}$  and temperature  $T$  fields are simulated, in our case with Pflotran [22], until a quasi-steady state is reached after  $\approx 27.5$  years simulated time [45]. All data are normalized to  $[0, 1]$ , and stored in PyTorch format for training.

We generate two types of datasets, one is based on synthetic, the other on real permeability fields  $k$ . Both cover a  $12.8 \times 12.8 \text{ km}^2$  domain with  $2560 \times 2560$  cells. The **baseline dataset** uses Perlin noise [28] to generate random, heterogeneous  $k$ . Three simulations (*3dp*) with different fields for  $i$  and  $k$  are run, generating one datapoint each for training, validation, and testing, plus a simulation  $4\times$  larger to assess scalability. For training vanilla neural networks in Section 4, we generate an additional dataset of 101 datapoints (*101dp*), split into 73:18:10 for train:val:test. Runtimes are  $\approx 27$  hours per simulation and 123 hours for the larger domain.

The more **realistic dataset** builds on  $k$  fields cut from maps of borehole measurements in the Munich region [4]. This dataset consists of four simulations (three for training and one for validation) and one larger simulation for testing scalability. Due to constraints of the available measurements, see Figure 1, the large-scale simulation extends only in length, resulting in a rectangular domain twice the length. Runtimes range from 38 to 91 hours (average 58 hours), and 134 hours for the scaling-test domain. Variation across the dataset stems from different heat pump placements in  $i$  and from the specific regions where  $k$  is extract from the available measurement domain.

For detailed information on simulation procedures and hydro-geological parameters, see Appendix A.1; for hardware specifications see Appendix A.4.

**Performance Metrics** We evaluate model accuracy per output dimension ( $v_x, v_y, T$ ) separately using Mean Absolute Error (MAE) [25], Mean Squared Error (MSE) [25], Maximum Absolute Error ( $L_\infty$ ) Structural Similarity Index Measure (SSIM) [47], and application-driven metrics of Percentage Above Threshold (PAT) and Visual Assessment. PAT measures the percentage of cells where the absolute error of the predicted temperature exceeds the threshold of  $0.1^\circ\text{C}$ , corresponding to measurement precision [44], and is only applicable to temperature predictions. All metrics other than SSIM are applied after re-normalization to the original data ranges to obtain physically meaningful results in  $[\text{C}]$  or  $[\text{meters/year}]$ .

## 4 Application of Purely Data-Driven Approaches

In this section, we present the performance of two purely data-driven approaches for predicting  $T$  from inputs of  $p, k, i$ : a UNet [35] and the domain-decomposition-based UNet variant, called DDUNet [46].

**Methods** The fully convolutional vanilla UNet has an encoder-decoder architecture with skip connections between layers of equal spatial dimensions. Convolutional networks excel in extracting local dependencies from spatial data with locally repeating patterns. Hence, in theory, one datapoint covering a large domain could be enough to generalize, if only local dependencies occur. Global patterns would require a large receptive field and, hence, more data. The DDUNet is designed to handle large-scale domains under GPU memory constraints. It combines a UNet architecture with domain decomposition principles by partitioning the spatial domain into subdomains that are distributed across multiple GPUs. We use a decomposition into  $2 \times 2$  subdomains.<sup>1</sup> Global context is communicated between subdomains via coarse feature maps through a learned communication network, maintaining spatial consistency and providing a large receptive field while reducing memory demands. The hyperparameters of the models are optimized according to Appendix A.2.1.

**Experiments** Experiments for the vanilla UNet are conducted on the baseline datasets with  $3dp$  and  $101dp$ , those with DDUNet directly on the  $101dp$  dataset, see Appendix A.3. Both models are applied to the test of  $3dp$  and to the scaling datapoint, for direct comparability to LGCNN. UNet exhibits poor performance when trained on the limited  $3dp$  dataset (UNet <sub>$3dp$</sub> ), as demonstrated in both Figure 4 and Table 1. Similar performance would be expected for the DDUNet when applied to this sparse dataset. When trained on  $101dp$ , however, both demonstrate robust predictive and scaling capabilities. The advantage of DDUNet over vanilla UNet is a reduction of memory usage and runtime, see appendix A.3.

Table 1: Performance metrics for predicting  $T$  from  $pki$  with UNet and DDUNet. Errors in  $[\text{C}]$ , MSE in  $[\text{C}^2]$ , PAT in  $[\%]$ , and SSIM unitless. Inferred on the test of  $3dp$  and the scaling datapoint.

Model	Test					Scaling				
	$L_\infty$	MAE	MSE	PAT	SSIM	$L_\infty$	MAE	MSE	PAT	SSIM
UNet <sub><math>3dp</math></sub>	4.8642	0.1314	0.0492	39.05	0.5794	–	–	–	–	–
UNet <sub><math>101dp</math></sub>	4.3985	0.0473	0.0100	13.63	0.9827	4.3426	0.0202	0.0033	4.33	0.9955
$2 \times 2$ -DDUNet <sub><math>101dp</math></sub>	3.4257	0.0548	0.0128	17.42	0.9804	4.1806	0.0235	0.0052	6.11	0.9940

## 5 Methodology

In data-scarce settings, performance can improve when the structure of a model reflects the underlying physics, cf. Section 2. This section hence outlines the relevant physical processes, motivates our LGCNN method, and discusses a few details of LGCNN’s individual components.

<sup>1</sup>Conceptually, DDUNet reduces to a standard UNet when trained with a single subdomain.



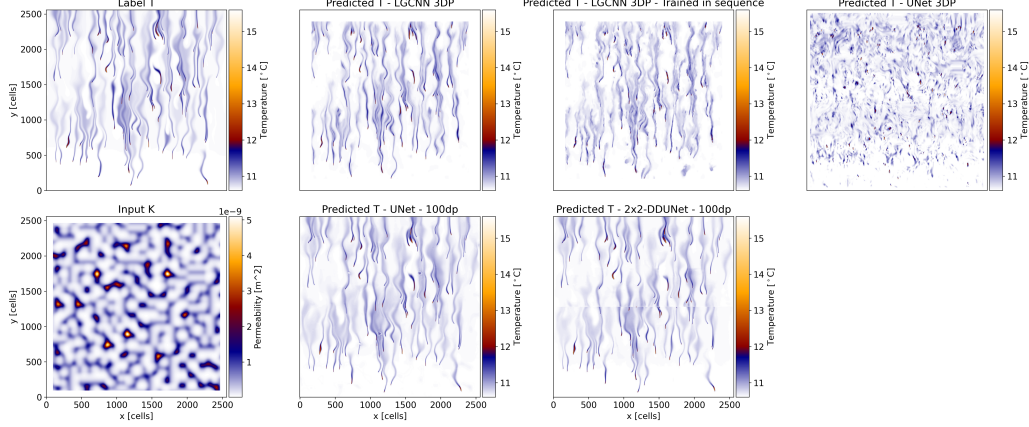


Figure 2:  $pki \rightarrow T$  (baseline dataset (3dp), test). 1st column: Label  $T$  and input  $k$ . 2nd-4th column: LGCNN<sub>3dp</sub> (isolated Step 3 and full pipeline, see Sections 5 and 6), vanilla UNet and DDUNet on 3dp and 101dp (Section 4).

**Physics of Groundwater Flow with Heat Transport** Transport of heat induced by heat injections of GWHPs in the subsurface is an advection–diffusion process. Since the Péclet number, i.e., the advection-diffusion ratio, is high in our application ( $Pe \gg 1$ , more in Appendix A.1), the system is advection-dominated. Advection is largely governed by the global hydraulic pressure gradient, driving flow from higher to lower regions. Locally, the flow paths are influenced by the spatial distribution of permeability  $k$ , cf. Figure 2. As a result, small changes in  $k$  can lead to significant differences in flow paths further downstream, demonstrating high input sensitivity.

**One-Way Coupled Approach: Local-Global CNN (LGCNN)** In a fully coupled physical model, flow field computation and heat transport along streamlines [24] starting at heat pumps (advection) and their widening (diffusion) must be solved monolithically. By splitting effects into local and global and working with steady-state simulated  $\vec{v}$  during training, we can reduce the coupling to one direction without significant loss in accuracy. Our simplified physical pipeline consists of three steps: (1) compute a steady-state flow field  $\vec{v}$  from initial subsurface parameters  $p$  and  $k$ , with  $i$  encoding mass influx around GWHPs; (2) transport injected heat along streamlines governed by  $\vec{v}$  until quasi-steady state [45]; and (3) apply plume widening to these heat paths, informed by soil diffusivity and  $\vec{v}$ , to approximate diffusion effects. The resulting one-way coupled LGCNN approach (see Figure 1) can formally be described as:

**Step 1 Velocities (local)** We employ a CNN to predict the velocity field  $\vec{v} = (v_x, v_y)$  from  $p$ ,  $k$ , and  $i$ :

$$\text{CNN}(p, k, i) = \vec{v}. \quad (1)$$

**Step 2 Streamlines (global)** Based on the predicted velocities  $\vec{v}$  from Step 1, we compute streamlines  $\vec{s}$  originating from all pump locations in  $i$  with an initial value problem (IVP) solver:

$$\text{IVP}(i, \vec{v}) = \vec{s}. \quad (2)$$

**Step 3 Temperature (local)** A second CNN predicts the temperature field  $T$  from the initial inputs  $p$ ,  $k$ ,  $i$ , the predicted velocities  $\vec{v}$  of Step 1 and streamlines  $\vec{s}$  calculated in Step 2:

$$\text{CNN}(p, k, i, \vec{v}, \vec{s}) = T. \quad (3)$$

The model outputs the steady-state temperature field  $T$  and, using the same inputs  $p$ ,  $k$ , and  $i$  as a simulation, serves as its direct surrogate.

**CNN Models in the Local Steps** The local Steps 1 and 3 are approximated by a UNet [35, 27], see Appendix A.2 for details of our architecture. It is beneficial to omit zero-padding to enforce shift invariance and reliance on purely local information; this approach is also validated by Islam et

al. in [16]. Due to the input sensitivity of the entire problem, each step is trained independently on simulated input data. In particular, the CNN in Step 3 is trained on the simulated velocities  $\vec{v}_{\text{sim}}$  and streamlines based on these fields. Only during inference, all steps are applied sequentially, i.e., Step 3 uses the outputs of Steps 1 and 2, including the predicted  $\vec{v}_{\text{pred}}$  as inputs.

The training is accelerated by partitioning the data into overlapping patches, which increases the effective number of datapoints while reducing their spatial size. Combined with the streamlines’ embedding and localizing of global flow patterns for the fully convolutional (locally) acting CNN, this training data enrichment allows the model to train effectively on very little data, sometimes as little as a single simulation run, while generalizing to unseen and even to larger domains. Validation and testing are conducted on independent simulation runs, with the full domain being processed as a whole instead of patches during inference.

The architecture, input choices, and training hyperparameters — including the patch size and overlap in the datapoint partitioning — were optimized through a combination of manual and automated tree-based search using Optuna [1]; see Appendix A.2.1 for details.

**Streamline Calculation and 2D-Embedding in the Global Step** Streamlines are calculated by solving the initial value problem (IVP)

$$\frac{dy}{dt} = \vec{v}(y), \text{ with } y(t_0) = y_0, \quad (4)$$

with a lightweight numerical solver for each heat pump, where  $y_0$  represents the location of a heat pump in  $i$ . We employ the `solve_ivp` function from SciPy [39] with an implicit fifth-order Runge-Kutta method [30] and 10 000 time steps of one day, corresponding to the simulation time of forming a heat plume.

The computed streamlines  $y$  represent a sequence of positions in 2D, that a particle - injected at a heat pump’s location - would traverse based on  $\vec{v}$ . The corresponding grid cells are assigned values that fade linearly from 1 to 0, reflecting the time it takes to reach each position, similar to a soft one-hot encoding.

To address the sensitivity of this process with respect to  $k$  and  $\vec{v}$ , we calculate a set of outer streamlines  $s_o$ . For this, we perturb each heat pump’s location  $y_0$  by 10 cells orthogonal to the global flow direction, i.e.,  $\nabla p$ , and compute the corresponding streamlines. By incorporating  $\vec{s} = (s, s_o)$ , the subsequent Step 3 obtains a spatial, localized representation of flow paths. In future work, we aim to explore probabilistic perturbations to compute the mean and standard deviation of streamlines, which, while being computationally more expensive, could be efficiently parallelized on GPUs.

## 6 Results on Synthetic Permeability Fields

This section evaluates our model’s performance on the baseline dataset *3dp* and on a scaling test datapoint; cf. Section 3. In Section 6.1, we present metrics for isolated velocity (Step 1) and temperature (Step 3) predictions, and for the full pipeline, demonstrating the potential of our approach. In ablation studies (Section 6.2), we motivate model design choices. Additional metrics and visualizations can be found in Appendix A.3.

### 6.1 Performance of LGCNN

**Isolated Steps 1 and 3** Performance metrics for Step 1 are shown in Table 2, for Step 3 (trained and tested on simulated  $\vec{v}_{\text{sim}}$ ) in Table 3. The combination of quantitative (MAE of (22.3, 32.7) m/y and 0.03 °C) and qualitative results through a visual assessment of Figure 3 demonstrate a strong performance with heat plumes forming according to  $k$ .

**Full Pipeline** Testing the full pipeline, i.e., Steps 2 and 3 are based on  $\vec{v}_{\text{pred}}$ , results in a higher test MAE of 0.09 °C compared to an isolated Step 3 (see Table 3). This was expected as the isolated Step 3 uses the true, simulated velocity fields  $\vec{v}_{\text{sim}}$  as inputs. Visual assessment of representative predictions in Figure 2 reveals physically plausible heat plumes in terms of shape, extent, and heat magnitude. Deviations in streamlines arise from smaller errors in the velocity predictions from Step 1  $\vec{v}_{\text{pred}}$ , highlighting the input sensitivity, especially near bifurcations, where small perturbations in  $\vec{v}$

Table 2: Metrics for predicting  $\vec{v}_{\text{pred}}$  in Step 1 and in ablation studies of Step 1 on test and on scaling data from our baseline  $3dp$  dataset with random  $k$ . In [m/y], except for MSE in [m<sup>2</sup>/y<sup>2</sup>], SSIM unitless.

	Output	Case	$L_\infty$	MAE	MSE	SSIM
LGCNN	<b>Step 1</b>					
	$v_x$	test	190.8046	22.3178	972.5668	0.9911
	$v_y$	test	256.2519	32.7444	2031.3357	0.9812
	$v_x$	scaling	294.0457	24.9261	1204.1154	0.9911
	$v_y$	scaling	367.6891	26.2795	1463.8218	0.9820
Ablation study	Train without data partitioning					
	$v_x$	test	202.6397	23.8584	1144.4479	0.9913
	$v_y$	test	332.9557	35.9249	2490.4104	0.9789
	Replace Step 1 with UNet <sub>101dp</sub>					
	$v_x$	test	1047.8464	12.7036	896.2758	0.9016
	$v_y$	test	2594.9504	14.3878	2317.6863	0.9903
	$v_x$	scaling	659.8439	5.2152	79.2508	0.9699
	$v_y$	scaling	456.1904	5.7492	83.9735	0.9948
	Replace Step 1 with $2 \times 2$ -DDUNet <sub>101dp</sub>					
	$v_x$	test	2453.5881	13.6735	1367.9061	0.9325
	$v_y$	test	2029.0269	15.1332	2221.4226	0.9919
	$v_x$	scaling	421.4186	8.1184	125.9511	0.9314
	$v_y$	scaling	400.2490	7.4200	135.7929	0.9955

Table 3: Metrics for predicting  $T$  in Step 3, in the full pipeline, and in ablations studies of Step 3 on test and on scaling data from our baseline  $3dp$  dataset with random  $k$ . In [°C], except for MSE in [°C<sup>2</sup>], PAT in [%], SSIM unitless.

	Case	$L_\infty$	MAE	MSE	PAT	SSIM
LGCNN	<b>Step 3, i.e., test on <math>\vec{v}_{\text{sim}}</math></b>					
	test	2.8990	0.0347	0.0041	7.54	0.9304
	scaling	3.0250	0.0168	0.0014	2.05	0.9510
	<b>Pipeline, i.e., test on <math>\vec{v}_{\text{pred}}</math></b>					
	test	4.2120	0.0905	0.0307	28.92	0.7637
Ablation study	scaling	4.9366	0.0413	0.0141	10.87	0.8654
	Train in sequence					
	test	4.0804	0.0901	0.0289	29.44	0.7553
	Include zero-padding					
	test	2.3391	0.0418	0.0048	9.19	0.8838
	Train without data partitioning					
	test	3.6420	0.0351	0.0043	7.41	0.9245
	Replace Step 3 with UNet <sub>101dp</sub>					
	test	4.4658	0.0416	0.0067	11.69	0.9835
	scaling	4.3489	0.0176	0.0022	3.07	0.9954
	Replace Step 3 with $2 \times 2$ -DDUNet <sub>101dp</sub>					
	test	4.2772	0.0376	0.0058	10.96	0.9915
	scaling	3.9946	0.0192	0.0025	4.73	0.9968

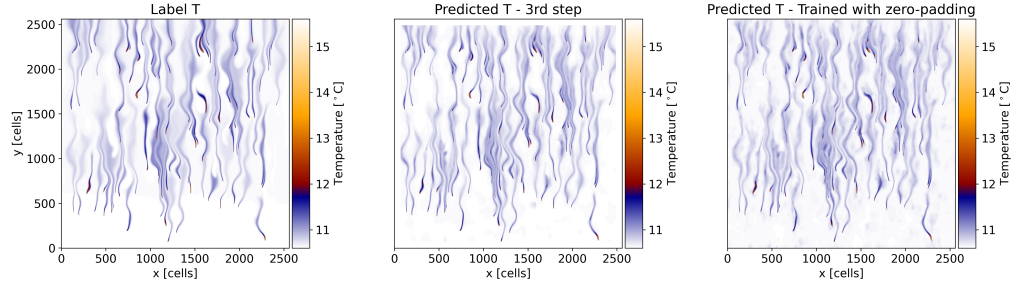


Figure 3:  $pkis\vec{v}_{\text{sim}} \rightarrow T$  (baseline dataset ( $3dp$ ), test). 1st column: Label  $T$ . 2nd-3rd column: LGCNN Step 3, trained without and with zero-padding.

can lead to an alternative path around a clay lens in  $k$ . Compared to fully data-driven models trained on  $101dp$  (see Table 1), our model achieves a similar accuracy while training on only 1 versus 73 training datapoints, which strongly reduces computation time (see Table 16 for details).

**Scaling Test** We can already expect that our model is able to scale to larger domains, as we train only on local patches of the spatial domain and achieve high test accuracies on the full domain during validation and testing; see also Section 6.2 *Training Data Partitioning* for more details. To further demonstrate the scaling, we test our model on a domain of  $4 \times$  the size of the training domain with the same number of heat pumps, hence with a lower density of GWHPs/km<sup>2</sup>; cf. Figure 4. We obtain a comparable MAE of 0.02 °C for Step 3, and an MAE of 0.04 °C for the full pipeline, see Table 3. A visual assessment of Figure 4 yields similar qualitative behavior as the previous results in Figure 2.

## 6.2 Ablation Study

**Training in Sequence** For training Step 3, we can either employ simulated  $\vec{v}_{\text{sim}}$  or predicted velocities  $\vec{v}_{\text{pred}}$  as inputs. As illustrated in Figure 2, training on  $\vec{v}_{\text{pred}}$  leads to physically implausible temperature fields with noisy artifacts and fragmented plumes. This likely stems from local misalign-

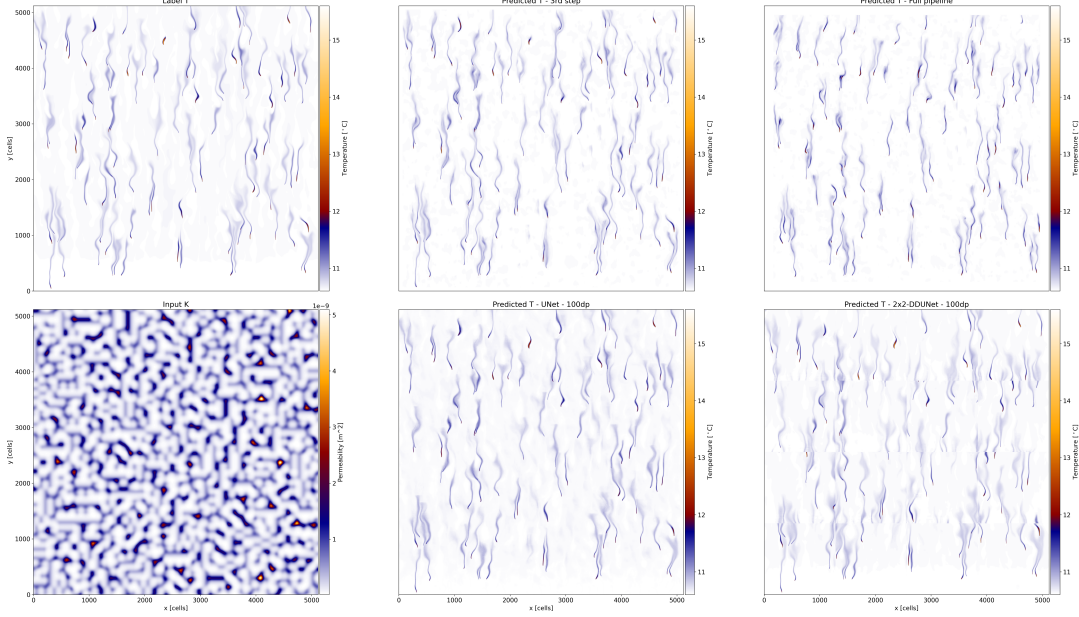


Figure 4:  $pki \rightarrow T$  (baseline dataset ( $3dp$ ), scaling). 1st column: Label  $T$  and input  $k$ . 2nd-3rd column: Comparison of LGCNN (isolated Step 3 and full pipeline) and vanilla data-driven architectures (UNet<sub>101dp</sub> and  $2 \times 2$ -DDUNet<sub>101dp</sub>).

ments between the inputs  $\vec{s}$  and  $\vec{v}_{\text{pred}}$ , and the corresponding label  $T$ , which strongly complicates localized training. Although loss values in Table 3 appear similar, the resulting temperature fields are less physically consistent and resemble those produced by end-to-end inference of UNet<sub>3dp</sub> in Section 4.

**Zero-Padding** Removing zero-padding from all convolutional layers yields smaller but cleaner output fields, as shown in Figure 3. As a result, we obtain improved performance, reflected in lower PAT and higher SSIM scores in Table 3.

**Partitioning Training Data** Hyperparameter search shows the best performance for partitioning the domain during training into 20 736 overlapping patches of  $256 \times 256$  cells for Step 1 and 82 944 patches for Step 3. Although this increases per-epoch compute time compared to full-domain training, it significantly reduces the number of epochs needed to reach comparable test performance (cf. Tables 2 and 3), resulting in an overall training time reduction of 67–90% (cf. Table 15).

**Replacing Isolated Steps with UNet<sub>101dp</sub> and  $2 \times 2$ -DDUNet<sub>101dp</sub>** We individually replace each of the three steps with an optimized (cf. Appendix A.2.1) vanilla approach, i.e., UNet or DDUNet trained on  $101dp$ . For Step 2, both fail completely; results for Steps 1 and 3 are summarized in Tables 2 and 3. In Step 1, UNet slightly outperforms DDUNet, while the reverse holds for Step 3. A visual comparison of the scaling datapoint in Figure 4 reveals that increasing training data from  $3dp$  to  $101dp$  has minimal impact on the performance in Step 3.

**Modifying Streamline Inputs of Step 3** We evaluate the influence of Step 3’s inputs, focusing on the effect of modifying or omitting individual components of the streamlines  $\vec{s} = (s, s_o)$ . When both the central streamlines  $s$  and offset streamlines  $s_o$  are excluded, predicted plumes fail to follow flow paths beyond the CNN’s receptive field. Omitting only  $s_o$  results in overly narrow plumes, whereas excluding only  $s$  produces overly smeared temperature fields. Including both but removing the fading of values along the streamlines leads to diffuse background temperatures and less localized plumes. Overall, the Huber validation loss increases by 32–132%, depending on the experiment. For visual, quantitative, and extended results, we refer to Appendix A.3.

## 7 Domain Transfer to Real Permeability Fields

Finally, we investigate whether our approach transfers to the realistic dataset in Section 3, which is based on real-world permeability fields  $k$  that are cut from geological maps of Munich. Since these maps cover a limited area, the number of potential datapoints is very small. We compare performance for temperature prediction of Step 3 and the full pipeline on the validation and scaling datapoints. Results are presented in Tables 4 and 5; additional metrics are in Appendix A.3.

Table 4: Metrics for predicting  $\vec{v}_{\text{pred}}$  in Step 1 on validation and scaling data from our realistic dataset. In [m/y], except for MSE in [m<sup>2</sup>/y<sup>2</sup>], SSIM unitless.

Output	Case	$L_\infty$	MAE	MSE	SSIM
<b>Step 1</b>					
$v_x$	val	106.8607	15.4095	380.3762	0.9939
$v_y$	val	74.5570	10.6605	148.2475	0.9993
$v_x$	scaling	459.1620	110.0078	13570.0000	0.9462
$v_y$	scaling	240.9406	17.6051	616.5186	0.9965

Table 5: Metrics for predicting  $T$  in Step 3 and in the full pipeline on validation and scaling data from our realistic dataset. In [°C], except for MSE in [°C<sup>2</sup>], PAT in [%], SSIM unitless.

Case	$L_\infty$	MAE	MSE	PAT	SSIM
<b>Step 3, i.e., test on <math>\vec{v}_{\text{sim}}</math></b>					
val	0.8222	0.0175	1.01e-3	2.18	0.9672
scaling	0.8052	0.0189	8.21e-4	0.92	0.9497
<b>Full pipeline, i.e., test on <math>\vec{v}_{\text{pred}}</math></b>					
val	2.3194	0.0841	2.75e-2	27.79	0.7510
scaling	2.0511	0.0394	4.42e-3	10.02	0.8708

**Methodological Adaptations** Slight adjustments to chunk size, overlap, data split, and architecture yield better performance compared to those used on the baseline dataset, see Appendix A.2.1 for details. Visual inspection of input  $k$  in Figure 5 reveals fewer but larger-scale features. Therefore, training can benefit from a larger spatial context, which requires more training data. We increase the number of training samples by using three out of the four available datapoints for training and one for validation. For the streamlines computation, we switch to an explicit fourth-order Runge–Kutta scheme, which proved stable and sufficient for training and inference due to the lower frequency in  $k$ .

**Performance and Scaling Tests** In Step 3, we reach an even lower maximum absolute error  $L_\infty$  of 0.82 °C compared to 2.90 °C of our initial model on the baseline dataset (Section 6). Other metrics confirm a similar performance; see Table 3. In the scaling test, most errors are comparable too. For the full pipeline, errors are slightly higher on the validation and scaling data compared to an isolated Step 3, consistent with our observations on the baseline dataset (Table 3). Physical consistency, which is our primary objective, remains strong: Shape, magnitude, and connectivity of the predicted heat plumes are well preserved, even in the scaling test (Figure 5). Local deviations are primarily due to differences between  $\vec{v}_{\text{sim}}$  and  $\vec{v}_{\text{pred}}$ , as evident from the discrepancy between Step 3 and full pipeline outputs.

## 8 Conclusions and Future Work

In real-world scientific applications, data is often very limited. At the same time, models are expected to generalize and scale to large domain sizes, pushing standard data-driven models to their limits. To address this issue, we proposed the LGCNN model, a hybrid, physics-inspired CNN approach. In the prediction of groundwater temperature fields under arbitrary heat pump configurations and real permeability data, we identify long-range interactions driven by advection as the problematic process for classical deep learning models, such as vanilla CNNs. We replace this part of the prediction with a simple numerical solver, resulting in a sequence (CNN 1 – numerical solver – CNN 2). While this setup is specific to groundwater heat transport, the general approach should be applied to a wider range of applications. Finally, we stress that traditional error metrics can obscure effects like input sensitivity; therefore, we additionally rely on visual assessments and problem-specific metrics such as PAT. In future work, we will address dataset limitations, investigate input sensitivity, and accelerate streamline computation.

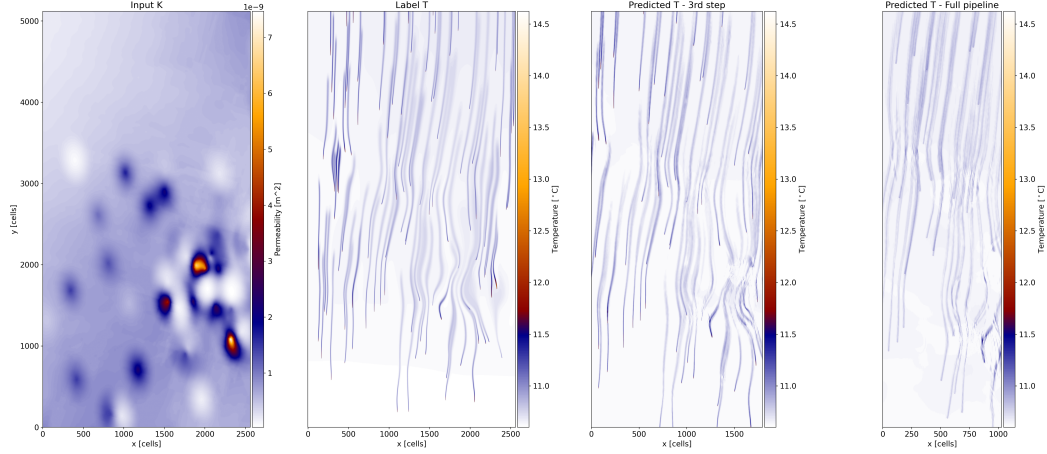


Figure 5:  $pki \rightarrow T$  (realistic dataset, scaling). 1st & 2nd column: Label  $T$  and input  $k$ . 3rd-4th column: LGCNN (isolated Step 3 and full pipeline).

## Acknowledgements

We thank the Deutsche Forschungsgemeinschaft (DFG, German Research Foundation) for supporting this work by funding - EXC2075 – 390740016 under Germany’s Excellence Strategy. We acknowledge the support by the Stuttgart Center for Simulation Science (SimTech). We also acknowledge the use of computational resources of the DelftBlue supercomputer, provided by Delft High Performance Computing Centre [10]. We thank Kai Zosseder and Fabian Böttcher at the Technical University of Munich for their application-related input.

## References

- [1] Takuya Akiba et al. “Optuna: A Next-generation Hyperparameter Optimization Framework”. In: *Proceedings of the 25th ACM SIGKDD International Conference on Knowledge Discovery and Data Mining*. 2019.
- [2] Mary P Anderson. “Introducing groundwater physics”. In: *Physics today* 60.5 (2007), pp. 42–47.
- [3] Sheena Angra and Sachin Ahuja. “Machine learning and its applications: A review”. In: *2017 international conference on big data analytics and computational intelligence (ICBDAC)*. IEEE. 2017, pp. 57–60.
- [4] Bayerisches Landesamt für Umwelt. *Geologische Daten: Geologisches Fachinformationssystem (GEPO)*. <https://www.lfu.bayern.de/geologie/gepo/index.htm>. Accessed: 2025-05-14. 2015.
- [5] Shengze Cai et al. *Physics-informed neural networks (PINNs) for fluid mechanics: A review*. arXiv:2105.09506 [physics]. May 2021. DOI: 10.48550/arXiv.2105.09506. URL: <http://arxiv.org/abs/2105.09506> (visited on 01/13/2023).
- [6] Byoung-Ju Choi, Hong Sung Jin, and Bataa Lkhagvasuren. “Applications of the Fourier neural operator in a regional ocean modeling and prediction”. In: *Frontiers in Marine Science* 11 (2024), p. 1383997.
- [7] Salvatore Cuomo et al. “Scientific machine learning through physics-informed neural networks: Where we are and what’s next”. In: *Journal of Scientific Computing* 92.3 (2022), p. 88.
- [8] Kyle Davis et al. *Deep learning based surrogate modeling for thermal plume prediction of groundwater heat pumps*. 2023. arXiv: 2302.08199 [physics.flu-dyn].
- [9] Jacques W Delleur. “Elementary groundwater flow and transport processes”. In: *The handbook of groundwater engineering*. CRC press, 2016, pp. 91–120.
- [10] Delft High Performance Computing Centre (DHPC). *DelftBlue Supercomputer (Phase 2)*. <https://www.tudelft.nl/dhpc/ark:/44463/DelftBluePhase2>. 2024.



- [11] US Department-of Energy. *Geothermal Heat Pumps – Energy Saver*. <https://www.energy.gov/energysaver/geothermal-heat-pumps>. Accessed: 2023-09-19. 2023.
- [12] M Giselle Fernández-Godino et al. “A Staged Deep Learning Approach to Spatial Refinement in 3D Temporal Atmospheric Transport”. In: *arXiv preprint arXiv:2412.10945* (2024).
- [13] *Geologica Bavarica Band 122: Die hydraulischen Grundwasserverhältnisse des quartären und des oberflächennahen tertiären Grundwasserleiters im Großraum München*. <https://www.bestellen.bayern.de/shoplink/91122.htm>. 2022.
- [14] Stefanie Hähnlein et al. “Sustainability and policy for the thermal use of shallow geothermal energy”. In: *Energy Policy* 59 (2013), pp. 914–925.
- [15] Quercus Hernández et al. “Structure-preserving neural networks”. In: *Journal of Computational Physics* 426 (2021), p. 109950.
- [16] Md Amirul Islam\*, Sen Jia\*, and Neil D. B. Bruce. “How much Position Information Do Convolutional Neural Networks Encode?”. In: *International Conference on Learning Representations*. 2020. URL: <https://openreview.net/forum?id=rJeB36NKvB>.
- [17] R. Jhaveri et al. “A Review on Machine Learning Strategies for Real-World Engineering Applications”. In: *Mobile Information Systems* (2022). DOI: 10.1155/2022/1833507.
- [18] Diederik P Kingma. “Adam: A method for stochastic optimization”. In: *arXiv preprint arXiv:1412.6980* (2014).
- [19] Aditi Krishnapriyan et al. “Characterizing possible failure modes in physics-informed neural networks”. In: *Advances in neural information processing systems* 34 (2021), pp. 26548–26560.
- [20] Zongyi Li et al. “Fourier neural operator for parametric partial differential equations”. In: *arXiv preprint arXiv:2010.08895* (2020).
- [21] Peter C Lichtner et al. *PFLOTRAN - Theory Guide - Thermal-Hydrologic Mode - Governing Equations*. Tech. rep. Accessed: 2025-03-12. Los Alamos National Lab.(LANL), Los Alamos, NM (United States); Sandia National Lab.(SNL-NM), Albuquerque, NM (United States); Lawrence Berkeley National Lab.(LBNL), Berkeley, CA (United States); Oak Ridge National Lab.(ORNL), Oak Ridge, TN (United States); OFM Research, Redmond, WA (United States), 2015.
- [22] Peter C Lichtner et al. *PFLOTRAN user manual: A massively parallel reactive flow and transport model for describing surface and subsurface processes*. Tech. rep. Accessed: 2023-09-19. Los Alamos National Lab.(LANL), Los Alamos, NM (United States); Sandia National Lab.(SNL-NM), Albuquerque, NM (United States); Lawrence Berkeley National Lab.(LBNL), Berkeley, CA (United States); Oak Ridge National Lab.(ORNL), Oak Ridge, TN (United States); OFM Research, Redmond, WA (United States), 2015.
- [23] Miguel Liu-Schiaffini et al. “Neural operators with localized integral and differential kernels”. In: *arXiv preprint arXiv:2402.16845* (2024).
- [24] NASA. *Definition of Streamlines*. <https://www.grc.nasa.gov/www/k-12/VirtualAero/BottleRocket/airplane/stream.html>. accessed on Aug 21, 2024.
- [25] MZ Naser and Amir H Alavi. “Error metrics and performance fitness indicators for artificial intelligence and machine learning in engineering and sciences”. In: *Architecture, Structures and Construction* 3.4 (2023), pp. 499–517.
- [26] Adam Paszke et al. “Automatic differentiation in PyTorch”. In: *NIPS-W*. 2017.
- [27] Julia Pelzer and Miriam Schulte. “Efficient Two-stage Modeling of Heat Plume Interactions of Geothermal Heat Pumps in Shallow Aquifers Using Convolutional Neural Networks”. In: *Geoenery Science and Engineering* 237 (2024), p. 212788.
- [28] Ken Perlin. “An image synthesizer”. In: *ACM Siggraph Computer Graphics* 19.3 (1985), pp. 287–296.
- [29] William Pophillat et al. “Impact of groundwater heat pump systems on subsurface temperature under variable advection, conduction and dispersion”. In: *Geothermics* 83 (2020), p. 101721.
- [30] *Radau – SciPy v1.15.3 Manual*. <https://docs.scipy.org/doc/scipy/reference/generated/scipy.integrate.Radau.html>. [Accessed 12-05-2025].

- [31] M. Raissi, P. Perdikaris, and G.E. Karniadakis. “Physics-informed neural networks: A deep learning framework for solving forward and inverse problems involving nonlinear partial differential equations”. In: *Journal of Computational Physics* 378 (2019), pp. 686–707. ISSN: 0021-9991. DOI: <https://doi.org/10.1016/j.jcp.2018.10.045>. URL: <https://www.sciencedirect.com/science/article/pii/S0021999118307125>.
- [32] Chengping Rao, Hao Sun, and Yang Liu. “Physics-informed Deep Learning for Incompressible Laminar Flows”. In: *Theoretical and Applied Mechanics Letters* 10.3 (2020), pp. 207–212.
- [33] Bastian E. Rapp. “Péclet Number”. In: *Microfluidics: Modelling, Mechanics and Mathematics*. Elsevier, 2017. Chap. 9.9.7. URL: <https://www.sciencedirect.com/topics/chemical-engineering/peclet-number>.
- [34] Olaf Ronneberger, Philipp Fischer, and Thomas Brox. “U-net: Convolutional networks for biomedical image segmentation”. In: *Medical image computing and computer-assisted intervention—MICCAI 2015: 18th international conference, Munich, Germany, October 5-9, 2015, proceedings, part III* 18. Springer, 2015, pp. 234–241.
- [35] Olaf Ronneberger, Philipp Fischer, and Thomas Brox. “U-Net: Convolutional Networks for Biomedical Image Segmentation”. In: *CoRR* abs/1505.04597 (2015). arXiv: 1505.04597. URL: <http://arxiv.org/abs/1505.04597>.
- [36] Iqbal H Sarker. “Machine learning: Algorithms, real-world applications and research directions”. In: *SN computer science* 2.3 (2021), p. 160.
- [37] Stefania Scheurer. *A deep learning approach for large-scale groundwater heat pump temperature prediction*. 2021. DOI: 10.18419/opus-12902.
- [38] Neha Sharma, Reecha Sharma, and Neeru Jindal. “Machine learning and deep learning applications-a vision”. In: *Global Transitions Proceedings* 2.1 (2021), pp. 24–28.
- [39] *solve\_ivp — SciPy v1.14.1 Manual*. [https://docs.scipy.org/doc/scipy/reference/generated/scipy.integrate.solve\\_ivp.html](https://docs.scipy.org/doc/scipy/reference/generated/scipy.integrate.solve_ivp.html). accessed on Aug 30, 2024.
- [40] Luning Sun et al. “Surrogate Modeling for Fluid Flows based on Physics-constrained Deep Learning without Simulation Data”. In: *Computer Methods in Applied Mechanics and Engineering* 361 (2020), p. 112732.
- [41] Makoto Takamoto et al. “Pdebench: An extensive benchmark for scientific machine learning”. In: *Advances in Neural Information Processing Systems* 35 (2022), pp. 1596–1611.
- [42] Bilal Thonnam Thodi, Sai Venkata Ramana Ambadipudi, and Saif Eddin Jabari. “Fourier neural operator for learning solutions to macroscopic traffic flow models: Application to the forward and inverse problems”. In: *Transportation research part C: emerging technologies* 160 (2024), p. 104500.
- [43] Nils Thuerey et al. “Deep Learning Methods for Reynolds-averaged Navier-Stokes Simulations of Airfoil Flows”. In: *AIAA Journal* 58.1 (2020), pp. 25–36.
- [44] UKB System Technology. *Kabellichtlot Typ 120 - LTC elektrische Leitfähigkeit bis 100m*. <https://geotechnik-shop.de/Kabellichtlot-Typ-120-LTC-elektrische-Leitfaehigkeit-bis-100m>. accessed on Aug 28, 2024.
- [45] Umweltministerium Baden-Württemberg. *Arbeitshilfe zum Leitfaden zur Nutzung von Erdwärme mit Grundwasserwärmepumpen für Ein- und Zweifamilienhäuser oder Anlagen mit Energieentzug bis zirka 45.000 kWh pro Jahr*. Accessed: 2023-03-13. 2009. URL: [https://um.baden-wuerttemberg.de/fileadmin/redaktion/m-um/intern/Dateien/Dokumente/5\\_Energie/Erneuerbare\\_Energien/Geothermie/4\\_Arbeitshilfe\\_zum\\_Leitfaden.pdf](https://um.baden-wuerttemberg.de/fileadmin/redaktion/m-um/intern/Dateien/Dokumente/5_Energie/Erneuerbare_Energien/Geothermie/4_Arbeitshilfe_zum_Leitfaden.pdf).
- [46] Corné Verburg, Alexander Heinlein, and Eric C. Cyr. “DDU-Net: A Domain Decomposition-Based CNN for High-Resolution Image Segmentation on Multiple GPUs”. In: *IEEE Access* 13 (2025), pp. 66967–66983. DOI: 10.1109/ACCESS.2025.3561033.
- [47] Zhou Wang et al. “Image quality assessment: from error visibility to structural similarity”. In: *IEEE Transactions on Image Processing* 13.4 (2004), pp. 600–612. DOI: 10.1109/TIP.2003.819861.
- [48] Maurice Weiler et al. *Equivariant and Coordinate Independent Convolutional Networks. A Gauge Field Theory of Neural Networks*. 2023. URL: [https://maurice-weiler.gitlab.io/cnn\\_book/EquivariantAndCoordinateIndependentCNNs.pdf](https://maurice-weiler.gitlab.io/cnn_book/EquivariantAndCoordinateIndependentCNNs.pdf).
- [49] Reza Yousefzadeh et al. “Determination of optimal oil well placement using deep learning under geological uncertainty”. In: *Geoenergy Science and Engineering* 246 (2025), p. 213621.



- [50] Ruiyang Zhang, Yang Liu, and Hao Sun. “Physics-guided convolutional neural network (PhyCNN) for data-driven seismic response modeling”. In: *Engineering Structures* 215 (2020), p. 110704.
- [51] Kai Zosseder et al. *Schlussbericht zum Verbundprojekt GEO-KW*. Tech. rep. Bundesministerium für Wirtschaft und Klimaschutz, 2022. DOI: 10.14459/2022md1692003.

## Data and Code Accessibility

Our raw data and pretrained models are publicly available on DaRUS [https://darus.uni-stuttgart.de/dataverse/ipvs\\_lgcnn/](https://darus.uni-stuttgart.de/dataverse/ipvs_lgcnn/) or more specifically:

Raw datasets:

- Raw dataset of random permeability with 3+1 datapoints ( $3dp + 1dp$ ): <https://doi.org/10.18419/darus-4156>
- Raw dataset of random permeability with 101 datapoints ( $101dp$ ): <https://doi.org/10.18419/darus-5064>
- Raw dataset of real permeability with 4+1 datapoints: <https://doi.org/10.18419/darus-5065>

Pretrained models (including hyperparameters):

- Models trained on random permeability fields,  $3dp$ : LGCNN, vanilla UNet $_{3dp}$ : <https://doi.org/10.18419/darus-5080>
- Vanilla approaches trained on random permeability fields,  $101dp$ : DDUNet $_{101dp}$ , UNet $_{101dp}$ , LGCNN experiment: replace isolated steps 1 and 3 with DDUNet $_{101dp}$ , UNet $_{101dp}$ : <https://doi.org/10.18419/darus-5081>
- LGCNN on real permeability fields,  $4dp$ : <https://doi.org/10.18419/darus-5082>

Our code for data generation (<https://github.com/JuliaPelzer/Dataset-generation-with-Pflotran>) and model training (including dataset preparation and evaluation routines) (for LGCNN and data preparation: <https://github.com/JuliaPelzer/Heat-Plume-Prediction/tree/AllIn1/LGCNN/release25>, for DDUNet: <https://github.com/corne00/DDUNetForHeatplumePrediction>) is on GitHub. Follow the instructions in the respective readme files to prepare the data and train or infer a model.

## A Appendix

### A.1 Simulation Setup and Transport Regime

In Section 3, we describe how the two datasets are generated using the subsurface simulation software Pflotran [22], which solves the coupled mass and energy conservation equations. Here, we provide additional technical details and modeling assumptions relevant for reproducibility. Furthermore, we show that for the selected parameters, the heat transport in our system is dominated by advection by a theoretical analysis.

**Hydro-geological, Operational and Simulation Parameters** Our data was generated on  $12.8\text{km} \times 12.8\text{km} \times 5\text{m}$  with a cell size of  $5\text{m} \times 5\text{m} \times 5\text{m}$  for the baseline simulations. To test scalability, we also simulate a domain that is twice as large in both  $x$ - and  $y$ -dimension for the baseline dataset, but only twice as large in  $y$ -dimension for the more realistic dataset due to dimension restrictions of the available input data.

The *baseline dataset* uses a constant hydraulic pressure gradient  $\nabla p$  of 0.003 [27, 13]; permeability field  $k$  is generated using Perlin noise [28] within  $(1.02\text{E-}11, 5.10\text{E-}9) \text{ m}^2$ , and 100 randomly placed heat pumps, which are all operating with a 5 i.e., C injection temperature difference compared to the surrounding groundwater and an injection rate of  $0.00024 \text{ m}^3/\text{s}$ . All values are based on realistic parameter ranges in the region of Munich [13, 51].

For the *realistic dataset*, instead of random permeability fields  $k$ , we use permeability field data that is derived from borehole measurements in the Munich region [4]. Furthermore, based on subsurface measurements, we set  $\nabla p = 0.0025$  for these simulations. All other simulation parameters remain identical to the baseline. Other subsurface and operational parameters are taken directly from [27], which also includes additional information about solver setup and boundaries. For mathematical details of the governing equations, we refer the reader to [21, 2, 9].

**Simplifications** For simplifications, we refer to the (hydraulic) pressure field  $p$  throughout the paper. In our paper, this field is the initial pressure field defined through the measured hydraulic head and is not the true pressure field at quasi-steady state with spatial details resulting from permeability  $k$  variations in the domain and mass injections at the heat pump positions. The true pressure field is only available after simulation (which we are avoiding for our approach) and strongly interacts with the velocity field.

**Péclet Number** To quantify whether heat transport in our system is dominated by advection or diffusion, we compute the dimensionless Péclet number [33], which is defined as

$$\text{Pe} = \frac{L \cdot v}{\alpha},$$

with the characteristic length  $L$ , the local velocity  $v$ , and the thermal diffusivity  $\alpha$ , defined as

$$\alpha = \frac{k}{\rho c_p},$$

with  $k$  the thermal conductivity,  $\rho$  the density, and  $c_p$  the specific heat capacity. We take the parameters of the solid phase of our simulation inputs of

- Thermal conductivity:  $k = 0.65 \text{ W}/(\text{m} \cdot \text{K})$
- Density:  $\rho = 2800 \text{ kg}/\text{m}^3$
- Specific heat capacity:  $c_p = 2000 \text{ J}/(\text{kg} \cdot \text{K})$

This yields a thermal diffusivity of:

$$\alpha = \frac{0.65}{2800 \cdot 2000} \approx 1.16 \times 10^{-7} \text{ m}^2/\text{s}$$

The velocity values are derived by simulations, taken in the direction of flow (longitudinal) from the realistic  $k$ -dataset:

- Maximum: 1200 m/year  $\approx 3.8 \times 10^{-5}$  m/s
- Minimum: 44 m/year  $\approx 1.4 \times 10^{-6}$  m/s
- Mean: 330 m/year  $\approx 1.04 \times 10^{-5}$  m/s

With a characteristic length determined by the heat plume length of 2000–6000 m and mean x-velocity, we get:

$$Pe = \frac{L \cdot v}{\alpha} \approx L \cdot 10^2 \approx 10^5$$

The interpretation of the Peclet number is given by the following:

- $Pe \ll 1$ : Diffusion dominates
- $Pe \approx 1$ : Diffusion and advection similarly dominate
- $Pe \gg 1$ : Advection dominates

Therefore,  $Pe \approx 10^5$  indicates that in the simulations, the heat transport is advection-dominated at larger scales.

## A.2 Neural Networks, Hyperparameters and Training Details

This section provides implementation and training details for all neural network models used in this work. We begin with a description of the baseline UNet architecture, which also forms the foundation of both LGCNN and DDU-Net. Then, we outline the hyperparameter optimization process and present the final configurations per model and dataset. All models are trained using PyTorch[26].

**UNet Architecture** The UNet architecture used in this work is based on the original design presented by Ronneberger et al. [34], with several modifications to tailor it to the specific needs of our task of predicting temperature fields. In this section, we introduce the key concepts that define the architecture and explain how they contribute to the model’s design. These concepts will be employed in the hyperparameter search to identify the most suitable configuration, taking into account memory and data limitations.

The UNet architecture essentially consists of a series of UNet blocks. Each block consists of the layers of "Convolution - Activation - Convolution - Norm - Activation - Convolution - Activation" with convolutional layers, a batch normalization layer, and activation functions. After each block, either an upsampling or a downsampling operation is applied via "Max Pooling 2D" or "Transposed Convolution 2D" with stride 2. The *depth* of the UNet refers to the number of UNet blocks in both the encoder and decoder. The *number of initial features* refers to the number of feature maps generated by the first downsampling block. Each downsampling block produces twice as many output feature maps as input feature maps, while each upsampling block reduces the number of feature maps by half. The *number of convolutions per block* denotes how many convolutional layers are applied within each block, while *kernel size* specifies the size of the kernels used in the convolutional operations. Additionally, we explore different activation functions (ReLU, tanh, sigmoid, and LeakyReLU) and various normalization strategies (batch normalization, group normalization, and no normalization). The UNet block exists in 2 variants, depending on the hyperparameter *repeat inner*: If *repeat inner* = False, the block looks like this "Convolution - Norm - Activation", if it is True, the block looks as described above.

The training process also involves several hyperparameters. The learning rate controls how quickly the model adjusts its parameters during training. The weight decay parameter helps prevent overfitting by penalizing large weights in the model. Furthermore, the Adam optimizer [18] is employed as *optimizer*. For the realistic permeability field, we additionally introduce the optimizable hyperparameter *optimizer switch*, which, when enabled, switches the optimizer to LBFGS after 90 epochs.

During inference, each datapoint is processed as a whole, but during training, they are loaded in smaller patches cut out from the datapoint. Optimized hyperparameters include their overlap, i.e., inverse of *skip per direction*, and their size, called *box length*. The data split is untouched by this, i.e. one simulation run per train / val / test separately. This is important to not overlap test patches with training ones.

### A.2.1 Hyperparameters and Hyperparameter Optimization

We optimize the hyperparameters of our architecture, training process and data loading in several rounds with Optuna [1] and additional manual tweaking. Optuna performs optimization using a tree-structured Parzen estimator algorithm. An overlook of all considered hyperparameters, their ranges and our final choice, as well as the hyperparameters fixed during optimization is provided per used model architecture and dataset, e.g., purely data-driven approaches, LGCNN on individual steps or the full pipeline, on datasets of random  $k$  versus realistic  $k$ .

**Vanilla UNet** The vanilla UNet<sub>3dp</sub> trained using the following hyperparameters: a batch size of 20, kernel size of 5, and a network depth of 3. The number of initial features was set to 32, with a stride and dilation of 1. We used the ReLU activation function in combination with batch normalization. The inner block was not repeated (`repeat_inner = False`). No cutouts are applied during training (`bool_cutouts = False`), i.e., the model is trained on the whole datapoint at once.

The inputs to the model are  $pki$  (pressure field, permeability field, and location of heat pumps). For training, the Mean Absolute Error (MAE) loss function was used, and optimized with the Adam optimizer. The learning rate is set to  $1 \times 10^{-5}$ . The model is trained for 10,000 epochs.

**Hyperparameters for purely data-driven approaches** The values considered during hyperparameter optimization for the UNet and DDUNet, trained on 73 datapoints and performed using Optuna [1], along with the best settings found, are listed in Table 6. Certain hyperparameters were fixed: we set the number of epochs to 750, with an early stopping criterion based on validation loss and a patience of 80 epochs. Additionally, we note that some hyperparameter combinations (e.g., 32 initial features, depth 6, and 3 convolutions per layer with a kernel size of 7) caused memory issues, leading to their exclusion from the hyperparameter search.

Table 6: Overview of used hyperparameters for the UNet<sub>101dp</sub> and  $2 \times 2$  DDUNet<sub>101dp</sub> their search ranges (if applicable), and best values across training stages. Note that the number of communicated feature maps in the vanilla UNet is simply an extra convolution layer in the coarsest part of the UNet (without communication).

Hyperparameter	Range	$pki \rightarrow v_x v_y$	(Step 1)	$kv_x v_y sso \rightarrow T$	(Step 3)	$pki \rightarrow T$	(Full)
		UNet <sub>101dp</sub>	$2 \times 2$ DDUNet <sub>101dp</sub>	UNet <sub>101dp</sub>	$2 \times 2$ DDUNet <sub>101dp</sub>	UNet <sub>101dp</sub>	$2 \times 2$ DDUNet <sub>101dp</sub>
<i>Dataset</i>							
Batch size (train)	4, 6, 8	4	6	6	4	6	6
Include pressure field	True, False	False	False	-	-	False	False
<i>Encoder-decoder properties</i>							
Depth	4, 5, 6	6	5	6	6	5	5
No. initial features	8, 16, 32	8	16	8	8	8	16
No. convs. per block	1, 2, 3	1	1	3	3	3	3
Kernel size	3, 5, 7	7	7	3	5	7	7
<i>Communication Network</i>							
No. comm. feature maps	64, 128, 256	64	128	256	64	256	256
<i>Training</i>							
Learning rate	[1e-5, 1e-3]	0.00024	0.00100	0.00017	0.00030	0.00024	0.00024
Weight decay	0.0, 0.001	0.0	0.0	0.0	0.0	0.0	0.0
Train loss	MSE, L1	MSE	MSE	L1	MSE	MSE	MSE

After the hyperparameter search, the values corresponding to the best-performing model (based on Huber loss for the validation dataset) were selected. With these values fixed, five models were trained using different randomly sampled initializations to evaluate sensitivity to random initialization, for these values see Tables 10 and 11.

**LGCNN Hyperparameters - on Random Permeability** The values considered during hyperparameter optimization with Optuna [1] and the best settings found for both steps of LGCNN are listed in Table 7. Although the optimization was originally run for 100 epochs, the optimum was consistently found within the first 25 epochs. Therefore, to reduce computation cost, we therefore conservatively lowered the maximum number of epochs to 50. This adjustment does not affect any of the reported metrics in the paper.

Table 7: LGCNN-Random  $k$ : Hyperparameter optimization: Parameter ranges and best configurations.

Parameter	Range	1st step	3rd step
<i>Parameters of the Dataset</i>			
inputs	$v : (p, i, k)$ $T : (i, v_x, v_y, s, s_o, k)$	$pik$	$iv_xv_yssok$
skip per direction	$v : 4, 8, 16, 32, 64$ $T : 8, 16, 32, 64$	16	8
box length	64, 128, 256, 512	256	256
<i>Parameters of Training</i>			
loss function (training)	MAE, MSE	MSE	MAE
optimizer	Adam, SGD	Adam	Adam
<i>Parameters of the Network</i>			
No. initial features	8, 16, 32, 64, 128	32	32
kernel size	3, 4, 5	5	4
depth	$v : 1, 2, 3, 4$ $T : 1, 2, 3$	4	4

Fixed parameters for this hyperparameter search are the learning rate (fixed at  $10^{-4}$ ), ReLU as activation function, the batch size of 20, and the use of a batch normalization layer within the inner blocks of the UNet architecture. The validation loss used for selecting the optimal model is the MAE.

**LGCNN Hyperparameters - on Real Permeability** The values considered during hyperparameter optimization on the dataset with a more realistic permeability field were selected using Optuna [1], and are summarized in Table 8, along with the best configurations found for both steps of the LGCNN. The optimization was run for up to 100 epochs. For more background on the network architecture and the various hyperparameters, cf. A.2. Several hyperparameters were fixed during this process. These include a constant learning rate schedule, an Adam optimizer with a weight decay of  $10^{-4}$ , and, when enabled, a switch to LBFGS after 90 epochs. Fixed architectural parameters include a convolutional stride and dilation of 1. During training, the inputs were cut out from the full datapoints. For model comparison, the validation loss was consistently computed using the Huber loss.

### A.3 Additional Experimental Results

This section provides additional experimental results. While the main results section focused only on the test and scaling datasets, we also include here the metric values on the training and validation datasets. For completeness and easier comparison, the test and scaling metrics are re-listed as well.

**Purely data-driven UNet, DDU-Net: Metrics of training and ablation study** Table 9 presents all the metrics for predicting the temperature field directly from the inputs  $pki$  using a data-driven approach, evaluated on the training, validation, and test datasets. The results are provided for several models: (1) UNet trained on only 1 datapoint and tested and validated on 2 additional datapoints, (2) a UNet trained on 73 datapoints (73-18-10 train-validation-test split), and (3) a DDUNet trained on the same 73 datapoints dataset, operating on  $2 \times 2$  subdomains. Furthermore, to assess the model’s sensitivity to random initialization, the training of the same architecture was repeated five times for the most relevant models. Based on these repetitions, the mean and standard deviation of the performance metrics were computed using the following equations:

$$\bar{x} = \frac{1}{n} \sum_{i=1}^n x_i \quad \text{and} \quad \sigma = \sqrt{\frac{1}{n-1} \sum_{i=1}^n (x_i - \bar{x})^2}$$

where  $x_i$  denotes the metric value from the  $i$ -th training run, and  $n = 5$  is the number of runs. These results are summarized in Table 10 and Table 11. The choice of  $n = 5$  was made empirically to

Table 8: LGCNN-Real  $k$ : Hyperparameter optimization: Parameter ranges and best configurations.

Parameter	Range	model $\vec{v}$	model $T$
<i>Parameters of the Dataset</i>			
inputs	$v : ki, pik, gik, gk, pk$ $T : iv_x v_y ss_o k$	$pik$	$iv_x v_y ss_o k$
batch size	2, 4, 8, 16	8	8
skip per direction	256, 128, 64, 32, 16, 8	8	8
box length	1280, 640	1280	1280
<i>Parameters of Training</i>			
loss function (training)	MSE, MAE	MSE	MSE
optimizer switch	True, False	False	False
learning rate	1e-3, 5e-4, 1e-4, 5e-5	1e-3	1e-4
<i>Parameters of the Network</i>			
No. initial features	8, 16, 32	32	16
kernel size	3, 5	3	5
depth	4, 5, 6	5	6
repeat inner	True, False	False	False
activation function	relu, tanh, sigmoid, leakyrelu	relu	relu
layer norm	batch-, group-, None	batch-	batch-

balance computational effort and statistical reliability. The standard deviations in Tables 10 and 11 were used as validation: they are neither excessively large (indicating instability) nor unrealistically small (indicating insufficient sampling).

In addition to testing the UNet and DDUNet trained on 73 datapoints on the 10-point test dataset, we also evaluate these models on the same datapoint used to test the UNet<sub>3DP</sub>.

Table 9: Performance metrics for predicting  $T$  with different models and datasets. Errors in [°C], MSE in [°C], PATs in [%] and SSIM unitless. The LGCNN-test dataset corresponds to the 1 datapoint used for testing the LGCNN approach.

Model	Data	Case	Huber	$L_\infty$	MAE	MSE	PAT	SSIM
UNet <sub>3DP</sub>	randomK3	train	0.0020	2.4954	0.0404	0.0040	6.43	0.8281
		val	0.0269	5.2901	0.1365	0.0574	38.82	0.5717
		test	0.0235	4.8642	0.1314	0.0492	39.05	0.5794
UNet	rK101	train	0.0010	4.2443	0.0172	0.0021	2.34	0.9960
		val	0.0051	4.1972	0.0441	0.0106	12.68	0.9859
		test	0.0050	4.2140	0.0426	0.0104	11.90	0.9869
	*	LGCNN-test	0.0048	4.3985	0.0473	0.0100	13.63	0.9827
	*	scaling	0.0016	4.3426	0.0202	0.0033	4.33	0.9955
2×2-DDUNet	rK101	train	0.0018	3.8100	0.0236	0.0038	4.47	0.9940
		val	0.0079	4.0084	0.0550	0.0165	17.03	0.9825
		test	0.0076	3.7006	0.0549	0.0159	17.14	0.9835
	*	LGCNN-test	0.0063	3.4257	0.0548	0.0128	17.42	0.9804
	*	scaling	0.0025	4.1806	0.0235	0.0052	6.11	0.9940

**LGCNN: Metrics of training and ablation study** The results of the LGCNN and DDU-Net, evaluated on both synthetic and realistic permeability fields, for the training, validation, testing, and scaling datasets are shown in Table 12 (for Step 1 - predict  $\vec{v}_{pred}$ ) and Table 13 (for Step 3 - predict  $T$ ). The column "data" refers to the dataset that a model was trained on and applied to, i.e., "randomK" stands for the baseline dataset  $3dp$ , "randomK101" for  $101dp$ . An asterisk indicates that the model

Table 10: Statistics for predicting  $T$  with different models and datasets. Errors in [ $^{\circ}\text{C}$ ], MSE in [ $^{\circ}\text{C}$ ], PATs in [%] and SSIM unitless. The LGCNN-test dataset corresponds to the 1 datapoint used for testing the LGCNN approach. Mean  $\pm$  standard deviation reported.

Model	Data	Case	Huber	$L_{\infty}$	MAE	MSE	PAT	SSIM
UNet <sub>3dp</sub>	randomK3	train	0.0025 $\pm$ 0.0024	4.69 $\pm$ 0.17	0.0155 $\pm$ 0.0071	0.0063 $\pm$ 0.0062	1.92 $\pm$ 1.16	0.981 $\pm$ 0.012
		val	0.0219 $\pm$ 0.0008	4.89 $\pm$ 0.07	0.1114 $\pm$ 0.0023	0.0474 $\pm$ 0.0019	34.76 $\pm$ 0.99	0.696 $\pm$ 0.006
		test	0.0176 $\pm$ 0.0006	4.85 $\pm$ 0.09	0.1043 $\pm$ 0.0018	0.0368 $\pm$ 0.0015	34.76 $\pm$ 0.76	0.703 $\pm$ 0.006
UNet <sub>101dp</sub>	rK101	train	0.0011 $\pm$ 0.0002	4.37 $\pm$ 0.20	0.0182 $\pm$ 0.0020	0.0023 $\pm$ 0.0004	2.45 $\pm$ 0.27	0.995 $\pm$ 0.002
		val	0.0055 $\pm$ 0.0003	4.36 $\pm$ 0.16	0.0454 $\pm$ 0.0019	0.0114 $\pm$ 0.0006	12.96 $\pm$ 0.55	0.984 $\pm$ 0.002
		test	0.0052 $\pm$ 0.0003	4.35 $\pm$ 0.23	0.0441 $\pm$ 0.0019	0.0110 $\pm$ 0.0006	12.49 $\pm$ 0.48	0.985 $\pm$ 0.002
	*	LGCNN-test	0.0049 $\pm$ 0.0002	4.30 $\pm$ 0.16	0.0470 $\pm$ 0.0010	0.0102 $\pm$ 0.0004	13.51 $\pm$ 0.59	0.983 $\pm$ 0.002
	*	scaling	0.0017 $\pm$ 0.0001	4.48 $\pm$ 0.15	0.0208 $\pm$ 0.0014	0.0035 $\pm$ 0.0002	4.38 $\pm$ 0.17	0.995 $\pm$ 0.001
2 $\times$ 2-DDUNet <sub>101dp</sub>	rK101	train	0.0014 $\pm$ 0.0003	4.11 $\pm$ 0.25	0.0203 $\pm$ 0.0026	0.00300 $\pm$ 0.0007	3.24 $\pm$ 0.68	0.995 $\pm$ 0.001
		val	0.0079 $\pm$ 0.0002	4.20 $\pm$ 0.25	0.0564 $\pm$ 0.0008	0.01648 $\pm$ 0.0005	17.32 $\pm$ 0.22	0.981 $\pm$ 0.002
		test	0.0075 $\pm$ 0.0001	4.05 $\pm$ 0.22	0.0552 $\pm$ 0.0008	0.01580 $\pm$ 0.0002	16.94 $\pm$ 0.36	0.982 $\pm$ 0.001
	*	LGCNN-test	0.0057 $\pm$ 0.0003	4.00 $\pm$ 0.20	0.0526 $\pm$ 0.0015	0.01171 $\pm$ 0.0006	16.44 $\pm$ 0.63	0.981 $\pm$ 0.002
	*	scaling	0.0025 $\pm$ 0.0001	4.04 $\pm$ 0.20	0.0251 $\pm$ 0.0007	0.00514 $\pm$ 0.0002	6.39 $\pm$ 0.17	0.994 $\pm$ 0.001
LGCNN	randomK3 Step 3	train	0.0001 $\pm$ 0.0001	2.64 $\pm$ 0.18	0.0064 $\pm$ 0.0008	0.0003 $\pm$ 0.0001	0.29 $\pm$ 0.08	0.996 $\pm$ 0.001
		val	0.0032 $\pm$ 0.0001	2.49 $\pm$ 0.29	0.0413 $\pm$ 0.0008	0.0065 $\pm$ 0.0003	10.88 $\pm$ 0.35	0.912 $\pm$ 0.003
		test	0.0025 $\pm$ 0.0000	2.74 $\pm$ 0.33	0.0382 $\pm$ 0.0006	0.0049 $\pm$ 0.0001	9.44 $\pm$ 0.35	0.918 $\pm$ 0.003
		scaling	0.0008 $\pm$ 0.0000	3.03 $\pm$ 0.31	0.0179 $\pm$ 0.0006	0.0016 $\pm$ 0.0001	2.54 $\pm$ 0.14	0.946 $\pm$ 0.005

Table 11: Statistics for predicting  $\vec{v}$  with the randomK dataset. Errors in [m/y], MSE in [m<sup>2</sup>/y<sup>2</sup>], SSIM unitless. Mean  $\pm$  standard deviation reported.

Model	Data	Output	Case	Huber	$L_{\infty}$	MAE	MSE	SSIM
LGCNN	randomK3	$v_x$	train	14.11 $\pm$ 11.52	96.63 $\pm$ 23.29	14.60 $\pm$ 11.53	380.19 $\pm$ 529.31	0.997 $\pm$ 0.002
		$v_y$	train	14.30 $\pm$ 7.10	135.26 $\pm$ 20.36	14.80 $\pm$ 7.11	361.61 $\pm$ 296.21	0.991 $\pm$ 0.006
		$v_x$	val	28.23 $\pm$ 7.76	445.13 $\pm$ 35.50	28.72 $\pm$ 7.77	1601.10 $\pm$ 587.80	0.989 $\pm$ 0.003
		$v_y$	val	27.33 $\pm$ 2.25	343.35 $\pm$ 26.80	27.82 $\pm$ 2.25	1587.57 $\pm$ 252.10	0.982 $\pm$ 0.002
		$v_x$	test	26.94 $\pm$ 5.99	216.74 $\pm$ 18.92	27.44 $\pm$ 5.99	1368.52 $\pm$ 431.48	0.990 $\pm$ 0.002
		$v_y$	test	30.38 $\pm$ 6.18	249.11 $\pm$ 11.37	30.88 $\pm$ 6.18	1848.47 $\pm$ 637.10	0.982 $\pm$ 0.005
		$v_x$	scaling	27.89 $\pm$ 6.53	286.08 $\pm$ 22.96	28.38 $\pm$ 6.53	1486.23 $\pm$ 451.52	0.990 $\pm$ 0.002
		$v_y$	scaling	27.60 $\pm$ 2.43	328.80 $\pm$ 24.95	28.09 $\pm$ 2.43	1578.87 $\pm$ 258.66	0.979 $\pm$ 0.003
LGCNN	realK	$v_x$	train	29.66 $\pm$ 2.29	592.17 $\pm$ 37.66	30.16 $\pm$ 2.29	2326.33 $\pm$ 327.11	0.988 $\pm$ 0.005
		$v_y$	train	28.93 $\pm$ 5.47	397.09 $\pm$ 72.78	29.43 $\pm$ 5.47	1778.28 $\pm$ 551.97	0.997 $\pm$ 0.009
		$v_x$	val	22.17 $\pm$ 2.24	170.47 $\pm$ 9.75	22.66 $\pm$ 2.24	909.39 $\pm$ 139.94	0.988 $\pm$ 0.002
		$v_y$	val	20.20 $\pm$ 4.07	113.33 $\pm$ 12.37	20.70 $\pm$ 4.08	645.11 $\pm$ 221.50	0.997 $\pm$ 0.001
		$v_x$	scaling	79.33 $\pm$ 21.80	532.35 $\pm$ 140.50	79.83 $\pm$ 21.80	9404.62 $\pm$ 4048.09	0.953 $\pm$ 0.014
		$v_y$	scaling	53.39 $\pm$ 12.64	602.41 $\pm$ 128.79	53.89 $\pm$ 12.64	4621.25 $\pm$ 1755.50	0.980 $\pm$ 0.006

was evaluated on a dataset different from the one it was trained on. Mostly relevant for the vanilla approaches that are trained on *101dp* and applied to scaling and test of *3dp*.

**LGCNN+random  $k$ : Performance of Step 1** The model generally obtains good results in Figure 3, even for cells that are far away from injection points.

**LGCNN+random  $k$ : Experiment on Inputs to Step 3** Additional tests show that excluding other inputs, either  $i$  alone or both  $i$  and  $k$ , raises prediction error by 58–121%. We also evaluated alternative time-stepping schemes for solving the IVP. Replacing the 5th-order implicit Runge–Kutta method with explicit 2nd- or 4th-order schemes accelerates computation, but increases prediction error by 16–23%—a moderate degradation compared to the complete removal of streamline inputs. Nonetheless, we retain the implicit scheme for its superior accuracy and stability. Quantitative and qualitative results for the predictions are shown in Figure 7 and Table 14.

**LGCNN+realistic  $k$ : Performance of 3rd step and full pipeline** The qualitative performance is observable in Figure 8, where we see coherent streamlines and plume structures for both the isolated 3rd step and the full pipeline.

Table 12: Performance metrics for predicting  $\vec{v}$  with different models and datasets. Errors in [m/y], MSE in [m<sup>2</sup>/y<sup>2</sup>], SSIM unitless.

Model	Data	Output	Case	Huber	L <sub>∞</sub>	MAE	MSE	SSIM
1st Step								
LGCNN	randomK	$v_x$	train	9.4732	132.6672	9.9620	171.0032	0.9972
		$v_y$	train	11.4005	223.4601	11.8902	275.6190	0.9937
		$v_x$	val	22.2241	343.9907	22.7179	1102.3721	0.9905
		$v_y$	val	26.6078	274.8036	27.1026	1524.5099	0.9841
		$v_x$	test	21.8237	190.8046	22.3178	972.5668	0.9911
		$v_y$	test	32.2488	256.2519	32.7444	2031.3357	0.9812
	*	$v_x$	scaling	24.4314	294.0457	24.9261	1204.1154	0.9911
	*	$v_y$	scaling	25.7847	367.6891	26.2795	1463.8218	0.9820
Experiment: trained on full image								
LGCNN	randomK	$v_x$	train	3.1983	39.9380	3.6714	21.5058	0.9993
		$v_y$	train	3.0496	43.9018	3.5177	21.4905	0.9988
		$v_x$	val	25.2418	417.1447	25.7367	1421.6547	0.9896
		$v_y$	val	29.6294	276.8029	30.1247	1827.3134	0.9824
		$v_x$	test	23.3646	202.6397	23.8584	1144.4479	0.9913
		$v_y$	test	35.4289	332.9557	35.9249	2490.4104	0.9789
Replace with UNet-101dp, i.e., $1 \times 1$ subdomain-DDUNet, trained on 101 datapoints								
DDUNet	randomK101	$v_x$	train	3.5468	678.7761	4.0134	86.6731	0.9767
		$v_y$	train	4.1030	690.1506	4.5816	100.2767	0.9934
		$v_x$	val	3.8368	647.1833	4.3058	90.3292	0.9739
		$v_y$	val	4.3649	685.6656	4.8433	102.8601	0.9931
		$v_x$	test	3.6643	584.8119	4.1325	83.4062	0.9731
		$v_y$	test	4.1355	547.8865	4.6131	87.7819	0.9924
	*	$v_x$	LGCNN-test	12.2161	1047.8464	12.7036	896.2758	0.9016
	*	$v_y$	LGCNN-test	13.9033	2594.9504	14.3878	2317.6863	0.9903
	*	$v_x$	scaling	4.7412	659.8439	5.2152	79.2508	0.9699
	*	$v_y$	scaling	5.2686	456.1904	5.7492	83.9735	0.9948
Replace with 2x2-DDUNet-101dp, i.e., $2 \times 2$ subdomains								
DDUNet	randomK101	$v_x$	train	5.3928	422.4526	5.8815	57.6045	0.9580
		$v_y$	train	4.0476	696.2919	4.5116	58.8457	0.9972
		$v_x$	val	5.7663	471.6309	6.2545	76.4372	0.9552
		$v_y$	val	4.5085	644.1844	4.9751	71.5679	0.9973
		$v_x$	test	5.5847	319.9844	6.0735	59.2501	0.9526
		$v_y$	test	4.2292	535.0656	4.6948	54.5020	0.9972
	*	$v_x$	LGCNN-test	13.1829	2453.5881	13.6735	1367.9061	0.9325
	*	$v_y$	LGCNN-test	14.6481	2029.0269	15.1332	2221.4226	0.9919
	*	$v_x$	scaling	7.6311	421.4186	8.1184	125.9511	0.9314
	*	$v_y$	scaling	6.9406	400.2490	7.4200	135.7929	0.9955
Domain Transfer, i.e., to more realistic data								
LGCNN	realK	$v_x$	train	13.6890	122.7981	14.1819	340.6713	0.9973
		$v_y$	train	9.0680	71.2576	9.5619	126.7222	0.9991
		$v_x$	val	14.9187	106.8607	15.4095	380.3762	0.9939
		$v_y$	val	10.1675	74.5570	10.6605	148.2475	0.9993
	*	$v_x$	scaling	109.5079	459.1620	110.0078	13570.0000	0.9462
	*	$v_y$	scaling	17.1118	240.9406	17.6051	616.5186	0.9965



Table 13: Performance metrics for predicting  $T$  with different models and datasets. Errors in [ $^{\circ}\text{C}$ ], MSE in [ $^{\circ}\text{C}^2$ ], PATs in [%], SSIM unitless.

Model	Data	Case	Huber	$L_{\infty}$	MAE	MSE	PAT	SSIM
3rd Step: trained and applied to $v_{sim}$								
LGCNN	* randomK $v_{sim}$	train	1.87e-5	2.2536	0.0014	3.95e-5	0.03	0.9997
		val	0.0027	2.8857	0.0369	0.0054	8.61	0.9283
		test	0.0021	2.8990	0.0347	0.0041	7.54	0.9304
		scaling	0.0007	3.0250	0.0168	0.0014	2.05	0.9510
Full Pipeline, i.e., Step 3 trained on $v_{sim}$ , but applied to $v_{pred}$								
LGCNN	* randomK $v_{pred}$	train	0.0121	5.1006	0.0642	0.0272	18.17	0.8700
		val	0.0188	4.2264	0.0967	0.0411	28.96	0.7625
		test	0.0147	4.2120	0.0905	0.0307	28.92	0.7637
		scaling	0.0065	4.9366	0.0413	0.0141	10.87	0.8654
Experiments on 3rd Step								
Trained in sequence, i.e., trained on $v_{pred}$								
LGCNN	* randomK $v_{pred}$	train	0.0032	4.0750	0.0198	0.0068	3.73	0.9794
		val	0.0195	3.8178	0.1003	0.0423	30.46	0.7442
		test	0.0139	4.0804	0.0901	0.0289	29.44	0.7553
Trained with zero-padding								
LGCNN	* randomK $v_{sim}$	train	0.0002	1.8465	0.0140	0.0004	0.33	0.9518
		val	0.0032	2.9051	0.0465	0.0064	11.31	0.8686
		test	0.0024	2.3391	0.0418	0.0048	9.19	0.8838
Trained on full image								
LGCNN	* randomK $v_{sim}$	train	0.0002	3.5648	0.0022	0.0004	0.09	0.9992
		val	0.0027	3.5088	0.0375	0.0055	8.81	0.9217
		test	0.0021	3.6420	0.0351	0.0043	7.41	0.9245
Replace with UNet-101dp: Step 3 trained and applied on $v_{sim}$								
DDUNet	* rK101	train	0.0019	3.8491	0.0283	0.0038	5.35	0.9911
		val	0.0027	3.9381	0.0350	0.0055	8.89	0.9895
		test	0.0025	3.7999	0.0343	0.0052	8.50	0.9903
		LGCNN-test	0.0032	4.4658	0.0416	0.0067	11.69	0.9835
		scaling	0.0010	4.3489	0.0176	0.0022	3.07	0.9954
Replace with 2x2-DDUNet-101dp: Step 3 trained and applied on $v_{sim}$								
DDUNet	* rK101	train	0.0015	4.0624	0.0200	0.0032	3.44	0.9952
		val	0.0040	4.1863	0.0410	0.0083	12.54	0.9904
		test	0.0039	4.0807	0.0411	0.0081	12.67	0.9910
		LGCNN-test	0.0029	4.2772	0.0376	0.0058	10.96	0.9915
		scaling	0.0012	3.9946	0.0192	0.0025	4.73	0.9968
Domain Transfer, i.e. to more realistic data								
3rd Step								
LGCNN	* realK $v_{sim}$	train	0.0002	0.7704	0.0139	0.0005	0.43	2.9107
		val	0.0005	0.8222	0.0175	0.0010	2.18	0.9672
		scaling	0.0004	0.8052	0.0189	0.0008	0.92	0.9497
Full Pipeline								
LGCNN	* realK $v_{pred}$	train	0.0049	2.5437	0.0534	0.0100	17.58	2.4923
		val	0.0137	2.3194	0.0841	0.0275	27.79	0.7510
		scaling	0.0022	2.0511	0.0394	0.0044	10.02	0.8708

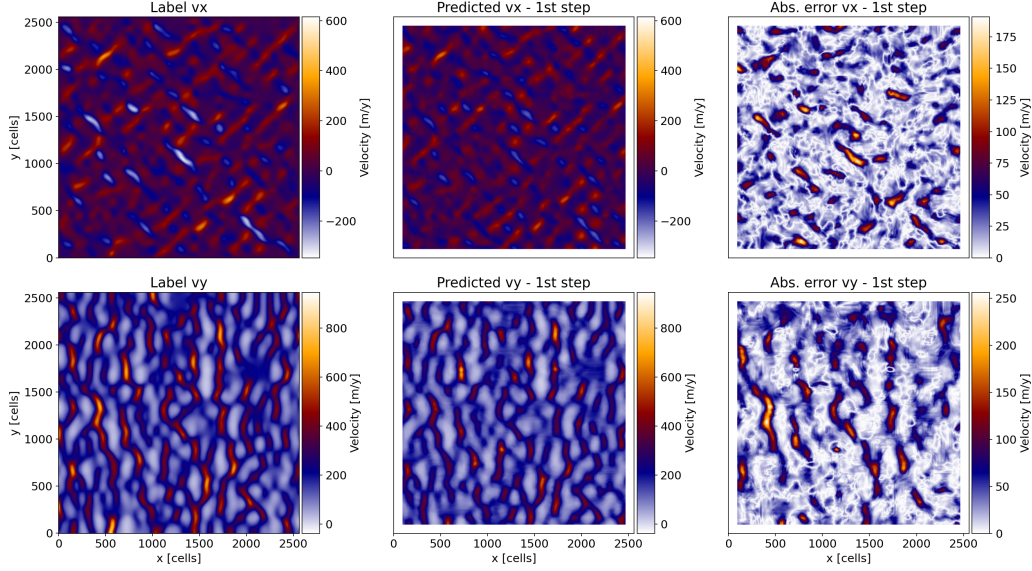


Figure 6: Prediction of  $\vec{v}$  with LGCNN. Left: Test datapoint with labels  $v_x$  and  $v_y$ . Middle: Step 1 prediction for  $v_x, v_y$ . Right: Error of the  $v_x, v_y$  prediction.

Table 14: Experiment on 3rd step: Test metrics for predicting  $T$  with different input combinations. Errors in [ $^{\circ}\text{C}$ ], MSE in [ $^{\circ}\text{C}^2$ ], PAT in [%], SSIM unitless.

Inputs	Huber	$L_{\infty}$	MAE	MSE	PAT	SSIM
$ikv_x v_y$	0.0070	2.2990	0.0712	0.0139	25.55	0.7662
$ikv_x v_y s$	0.0041	1.8674	0.0545	0.0083	20.56	0.8368
$ikv_x v_y s_o$	0.0057	2.6623	0.0598	0.0114	20.64	0.8423
$ikv_x v_y s s_o$ (not faded)	0.0072	2.3039	0.0744	0.0144	21.40	0.7837
$ikv_x v_y s s_o^a$	0.0031	1.8364	0.0442	0.0062	12.97	0.8828
$v_x v_y s s_o$	0.0066	2.1301	0.0647	0.0132	20.64	0.8681
$kv_x v_y s s_o$	0.0049	2.0925	0.0587	0.0097	20.32	0.8732
explicit RK, order 4	0.0038	3.2636	0.0486	0.0076	15.80	0.8871
explicit RK, order 2	0.0036	2.2034	0.0463	0.0072	13.75	0.8830

<sup>a</sup> new run to be comparable to the others in this experiment: trained with Huber validation loss, hence the results differ slightly wrt. to Table 3.

**Training and inference times** Table 15 summarizes the training and inference times, number of epochs, and dataset splits (train:val:test) for each of the three steps in our pipeline, both for the LGCNN trained on partitioned and full datasets. Although both approaches exhibit similar inference times, they show significant differences in training time, with the partitioned approach yielding better results.

Table 15: Training measurements on the randomK dataset.

	Data Points (train:val:test)	Epochs <sup>a</sup>	Training Time <sup>a</sup>	Inference Time
1st Step (partitioned)	20,736:1:1	19	9.5 min	0.02 s
1st Step (full)	1:1:1	9,688	92.6 min	0.02 s
2nd Step	1:1:1	-	-	9.82 s
3rd Step (partitioned)	82,944:1:1	14	31.5 min	0.03 s
3rd Step (full)	1:1:1	9,671	92.1 min	0.02 s

<sup>a</sup>Early stopping: measurements until best validation loss.

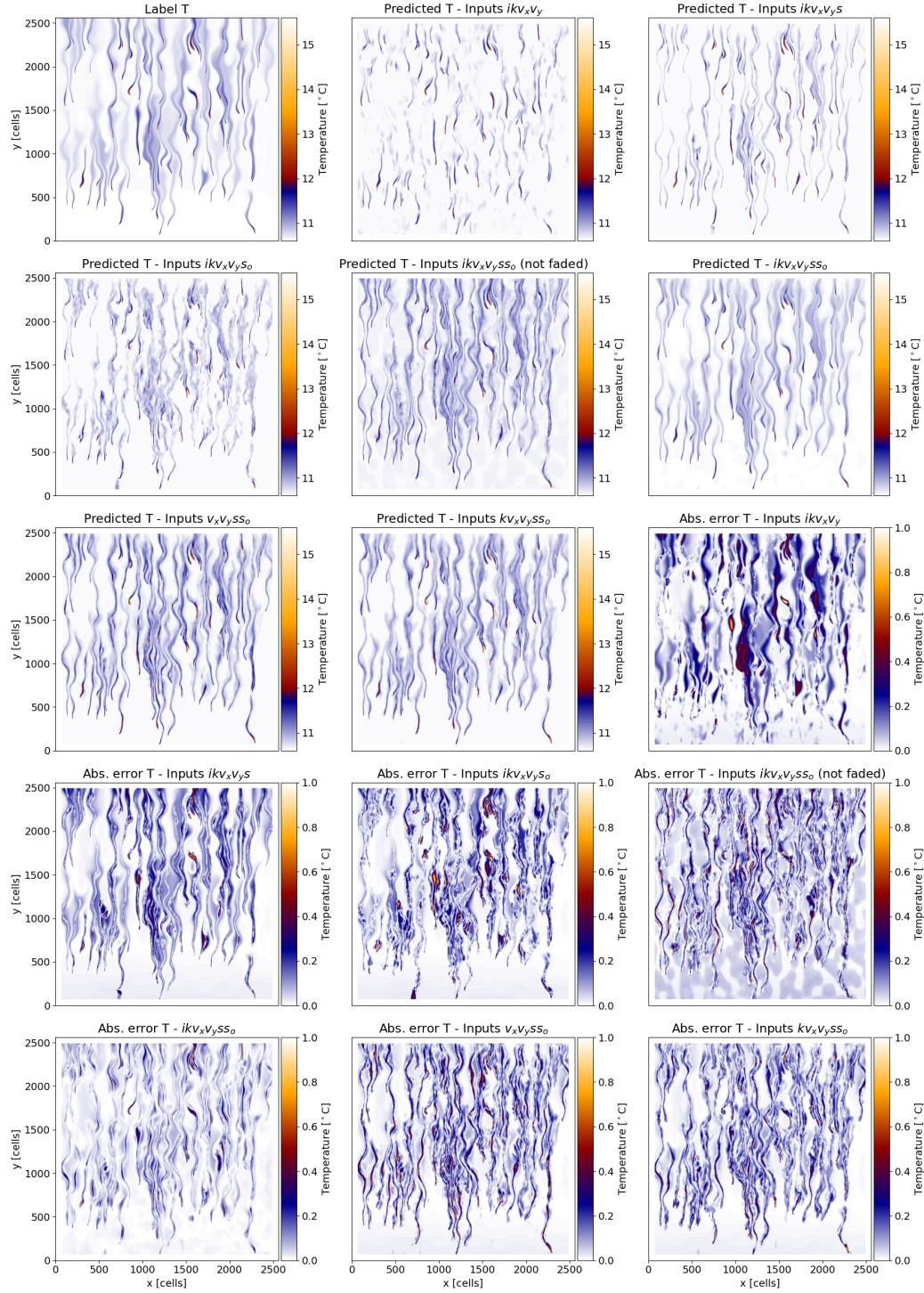


Figure 7: 1st Column: Label, input  $k$ , 2nd-5th: Without  $(s, s_o)$ ,  $(s_o)$ ,  $(s)$ , not-faded streamlines  $(s, s_o)$ , 6th: include all inputs, 7th-8th: Without  $(i, k)$ ,  $(i)$ . Absolute errors capped at  $1^\circ\text{C}$  for better visualizations. Maximum errors are listed in Table 14.

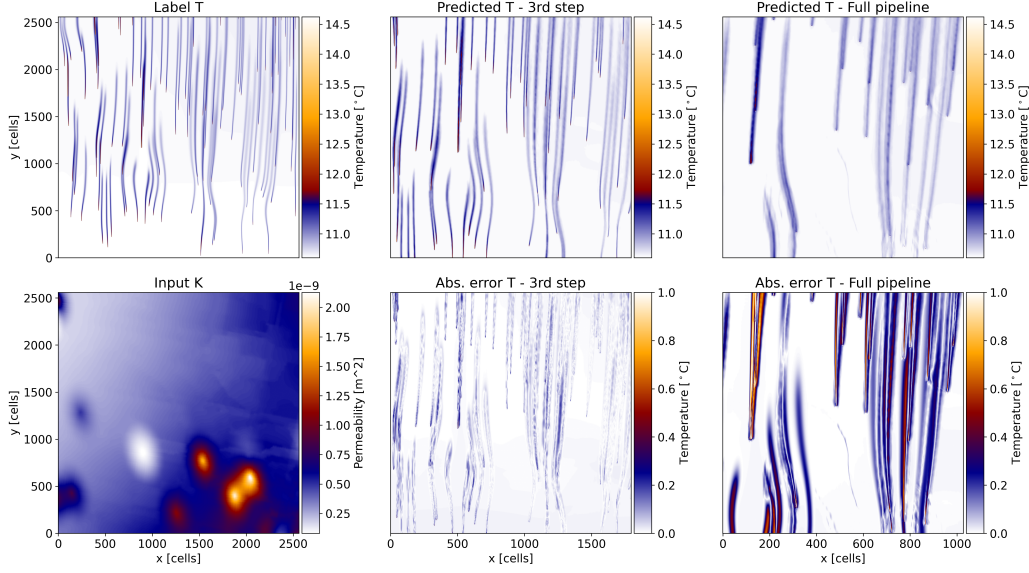


Figure 8: 1st Column: Label, input  $k$ . 2nd Column: 3rd step prediction of  $T$  and error with respect to the label. 3rd Column: Predicted  $T$  and error of the full pipeline.

In Table 16, the number of epochs and the total training time for the data-driven approaches are shown. For Step 1, both the UNet and DDUNet need many epochs and comparable training time to converge; however, for the third step and the full pipeline, the DDUNet significantly reduces both the number of epochs and the total training time required to reach convergence.

Table 16: Training measurements for the data-driven approaches trained on the  $101dp$  dataset: UNet $_{101dp}$  and  $2 \times 2$  DDUNet $_{101dp}$ .

	Epochs <sup>a</sup>	Training Time <sup>a</sup>
<b>1st Step</b>		
UNet $_{101dp}$	738	5.497 hours
$2 \times 2$ DDUNet $_{101dp}$	735	4.787 hours
<b>3rd Step</b>		
UNet $_{101dp}$	726	8.343 hours
$2 \times 2$ DDUNet $_{101dp}$	303	3.508 hours
<b>Full Pipeline</b>		
UNet $_{101dp}$	267	3.680 hours
$2 \times 2$ DDUNet $_{101dp}$	97	1.222 hours

<sup>a</sup>Early stopping: measurements until best validation loss.

#### A.4 Hardware Specifications

The  $2 \times 2$  DDU-Net $_{101dp}$  and UNet $_{101dp}$  models, trained on the large data-driven dataset of 101 samples, were trained and evaluated on the DelftBlue cluster [10], using NVIDIA V100 GPUs with 32 GB memory. All training was conducted using PyTorch 2.1.0 with CUDA 11.6 acceleration.

Training and evaluation of the LGCNN model were performed on a single NVIDIA A100-SXM4 GPU. Data generation was carried out on a dual-socket system equipped with AMD EPYC 9274F CPUs.

#### A.5 Glossary

A list of the most relevant physical properties used in our paper is provided in Table 17.

Table 17: Glossary of Abbreviations.

Abbr.	Parameter
$t$	time
$X(t_0)$	property X at initial time
$X(t_{\text{end}})$	property X at quasi steady-state
$X_{\text{pred}}$	predicted property X
$i$	positions of heat pumps
$Q_{\text{inj}}$	injected mass rate
$\Delta T_{\text{inj}}$	injected temperature difference
$k$	permeability
$p$	hydraulic pressure
$g = \nabla p$	hydraulic pressure gradient
$\vec{v} = (v_x, v_y)$	flow velocity
$\vec{s}$	both streamline fields
$s$	central streamlines after all $i$
$s_o$	streamlines with transversal offset to $i$
$T$	temperature